FERMILAB-PUB-24-0714-PPD

Searches for CEνNS and Physics beyond the Standard Model using Skipper-CCDs at CONNIE

Alexis A. Aguilar-Arevalo, Juan Carlos D'Olivo, and Y. Sarkis
Instituto de Ciencias Nucleares, Universidad Nacional Autónoma de México, Circuito Exterior s/n, C.U., CDMX, Mexico

Nicolas Avalos and Xavier Bertou
Centro Atómico Bariloche and Instituto Balseiro,
Comisión Nacional de Energía Atómica (CNEA),
Consejo Nacional de Investigaciones Científicas y Técnicas (CONICET),
Universidad Nacional de Cuyo (UNCUYO), Av Bustillo 9500, San Carlos de Bariloche, Argentina

Carla Bonifazi*
International Center for Advanced Studies & Instituto de Ciencias Físicas,
ECyT-UNSAM and CONICET, 25 de Mayo y Francia, Buenos Aires, Argentina and
Instituto de Física, Universidade Federal do Rio de Janeiro,
Av. Athos da Silveira Ramos, 149, Cidade Universitária, Rio de Janeiro, RJ, Brazil

Gustavo Cancelo, Juan Estrada, Richard Ford, Kevin Kuk, Andrew Lathrop, Javier Tiffenberg, and Sho Uemura
Fermi National Accelerator Laboratory, Batavia, IL, United States

Brenda A. Cervantes-Vergara
Instituto de Ciencias Nucleares, Universidad Nacional Autónoma de México,
Circuito Exterior s/n, C.U., CDMX, Mexico and
Fermi National Accelerator Laboratory, Batavia, IL, United States

Claudio Chavez
Fermi National Accelerator Laboratory, Batavia, IL, United States
Instituto de Inv. en Ing. Eléctrica "Alfredo Desages" (IIIE),
Dpto. de Ing. Eléctrica y de Computadoras, CONICET and Universidad Nacional del Sur (UNS),
800 San Andrés Street, Bahía Blanca, Argentina and
Facultad de Ingeniería, Universidad Nacional de Asunción, Campus de la UNA, San Lorenzo, Paraguay

Fernando Chierchie
Instituto de Inv. en Ing. Eléctrica "Alfredo Desages" (IIIE),
Dpto. de Ing. Eléctrica y de Computadoras, CONICET and Universidad Nacional del Sur (UNS),
800 San Andrés Street, Bahía Blanca, Argentina

Gustavo Coelho Corrêa
Eletronuclear, Rodovia Procurador Haroldo Fernandes Duarte km 521, Itaorna, Angra dos Reis, RJ, Brazil

João dos Anjos and Herman P. Lima Jr.
Centro Brasileiro de Pesquisas Físicas, Rua Dr. Xavier Sigaud, 150, Urca, Rio de Janeiro, RJ, Brazil

Guillermo Fernandez Moroni
Fermi National Accelerator Laboratory, Batavia, IL, United States and
Instituto de Inv. en Ing. Eléctrica "Alfredo Desages" (IIIE),
Dpto. de Ing. Eléctrica y de Computadoras, CONICET and Universidad Nacional del Sur (UNS),
800 San Andrés Street, Bahía Blanca, Argentina

Aldo R. Fernandes Neto
Centro Federal de Educação Tecnológica Celso Suckow da Fonseca,
Campus Angra dos Reis, Rua do Areal, 522, Pq Mambucaba, Angra dos Reis, RJ, Brazil

Ben Kilminster
Physik Institut, Universität Zürich, Winterthurerstrasse 190, Zurich, Switzerland

Patrick Lemos, Katherine Maslova, Irina Nasteva, Ana Carolina Oliveira, and Pedro Ventura
Instituto de Física, Universidade Federal do Rio de Janeiro,
Av. Athos da Silveira Ramos, 149, Cidade Universitária, Rio de Janeiro, RJ, Brazil

Martin Makler
International Center for Advanced Studies & Instituto de Ciencias Físicas, ECyT-UNSAM and CONICET, 25 de Mayo y Francia, Buenos Aires, Argentina and Centro Brasileiro de Pesquisas Físicas, Rua Dr. Xavier Sigaud, 150, Urca, Rio de Janeiro, RJ, Brazil

Franciole Marinho
Instituto Tecnológico de Aeronáutica, São José dos Campos, Brazil

Jorge Molina and Diego Stalder
Facultad de Ingeniería, Universidad Nacional de Asunción, Campus de la UNA, San Lorenzo, Paraguay

Laura Paulucci
Universidade Federal do ABC, Avenida dos Estados 5001, Santo André, SP, Brazil

Dario Rodrigues
Departamento de Física, FCEN, Universidad de Buenos Aires and IFIBA, CONICET, Pabellón I, Ciudad Universitaria, Buenos Aires, Argentina

Miguel Sofo-Haro
Universidad Nacional de Córdoba, CONICET (IFEG) and CNEA (RA0), Córdoba, Argentina
(CONNIE collaboration)
(Dated: March 26, 2024)

The Coherent Neutrino-Nucleus Interaction Experiment (CONNIE) aims to detect the coherent scattering (CEνNS) of reactor antineutrinos off silicon nuclei using thick fully-depleted high-resistivity silicon CCDs. Two Skipper-CCD sensors with sub-electron readout noise capability were installed at the experiment next to the Angra-2 reactor in 2021, making CONNIE the first experiment to employ Skipper-CCDs for reactor neutrino detection. We report on the performance of the Skipper-CCDs, the new data processing and data quality selection techniques and the event selection for CEνNS interactions, which enable CONNIE to reach a record low detection threshold of 15 eV. The data were collected over 300 days in $2021-2022$ and correspond to exposures of 14.9 g-days with the reactor-on and 3.5 g-days with the reactor-off. The difference between the reactor-on and off event rates shows no excess and yields upper limits at 95% confidence level for the neutrino interaction rates, comparable with previous CONNIE limits from standard CCDs and higher exposures. Searches for new neutrino interactions beyond the Standard Model were performed, yielding an improvement on the previous CONNIE limit on a simplified model with light vector mediators. A first dark matter (DM) search by diurnal modulation was performed by CONNIE and the results represent the best limits on the DM-electron scattering cross-section, obtained by a surface-level experiment. These promising results, obtained using a very small-mass sensor, illustrate the potential of Skipper-CCDs to probe rare neutrino interactions and motivate the plans to increase the detector mass in the near future.

I. INTRODUCTION

Coherent elastic neutrino-nucleus scattering (CEνNS) is an interaction process in which the neutrino scatters off the nucleus as a whole, benefiting from a coherent enhancement of the cross-section at low neutrino energies. Despite being predicted in the Standard Model (SM) over four decades ago [1], the process was only recently discovered for the first time, thanks to the development of ultra-sensitive detectors and pulsed sources of neutrinos from stopped pions. It was first observed by the COHERENT collaboration at the Spallation Neutron Source using a CsI[Na] scintillating crystal detector [2] in 2017, and was also detected later using a single-phase liquid argon (LAr) detector [3] and with a larger CsI[Na] dataset [4]. The observation of the process has opened up a new realm of possibilities for exploring neutrino physics at low energies.

Since the CEνNS interaction cross-section is predicted with precision in the SM, its measurement can be used to probe new physics in a number of possible scenarios. Non-standard interactions (NSI) of neutrinos [5–7], predicted by some extensions of the SM, can be explored at low energies by looking for enhancements of the measured coherent scattering rate due to additional neutral-current processes between quarks and neutrinos. Examples of possible searches include models with light scalar [8, 9] and vector boson mediators [10, 11], or pseudoscalar axionlike particles [12, 13], and there is a complementarity in NSI sensitivity between the measurements of stopped-pion and reactor experiments [14]. Measurements of CEνNS at short baselines can be used

* cbonifazi@unsam.edu.ar, bonifazi@if.ufrj.br

This document was prepared by CONNIE Collaboration using the resources of the Fermi National Accelerator Laboratory (Fermilab), a U.S. Department of Energy, Office of Science, Office of High Energy Physics HEP User Facility. Fermilab is managed by Fermi Research Alliance, LLC (FRA), acting under Contract No. DE-AC02-07CH11359.

to search for depletion in the flux due to oscillations into sterile neutrinos [15–17]. The process can also probe non-standard neutrino electromagnetic properties, such as millicharge [18] or charge radii [19]. Models with a neutrino anomalous magnetic moment, in which the neutrino-nucleus scattering is mediated by a light boson, predict a significant enhancement of the cross-section at low energies and could result in a several orders of magnitude increase in the event rates [20, 21].

The coherent scattering interaction can also be used to measure the weak mixing angle at low energies [22–24]. It can provide important information on nuclear structure by measuring the weak form factor, which depends on the neutron density distribution and can be used to measure the neutron radius and the neutron skin [25]. The process is also relevant to supernova energy transport and stellar collapse [26, 27] and direct dark matter detection where it is a limiting background [28, 29]. In terms of potential applications, in recent years the possibility to apply coherent scattering in non-invasive nuclear reactor and non-proliferation monitoring using neutrinos has been investigated [30, 31].

The recent intense developments in coherent scattering phenomenology and searches for physics beyond the SM have been accompanied closely by rich and varied experimental programmes. Detecting coherent elastic neutrino-nucleus scattering is very challenging due to the low neutrino energies involved, $E_\nu \lesssim 50$ MeV, and the even lower energies of the resulting nuclear recoils. Furthermore, only a fraction of these recoil energies generate a measurable signal such as ionisation, which is reflected in the quenching factors that measure ionisation efficiency as a function of nuclear recoil energy. Therefore the experimental efforts have focused on achieving ever lower energy thresholds and lower background rates, while striving to maximise the detector mass and neutrino flux available.

On the one hand, in terms of the experiments using stopped-pion neutrino sources, the COHERENT collaboration is taking data and preparing new detectors [32], while new CEνNS experiments are also being planned for the European Spallation Source [33]. On the other hand, several current and future experiments are using nuclear reactors as a high-flux neutrino source with the aim of detecting CEνNS. The reactor experiments employ a variety of different detection technologies: high-purity germanium crystal detectors in the CONUS [34], nuGEN [35], NCC-1701 [36] and TEXONO [37] experiments, liquid noble gas detectors in RED-100 [38], scintillating crystals in NEON [39], cryogenic bolometers and solid-state detectors in MINER [40], NUCLEUS [41] and RICOCHET [42], and silicon CCDs (charge coupled devices) in CONNIE and Atucha-II [43].

The Coherent Neutrino-Nucleus Interaction Experiment (CONNIE) seeks to detect the coherent scattering of reactor antineutrinos off silicon nuclei using thick fully-depleted high-resistivity silicon CCDs. The detector is operating in a ground-level laboratory adjacent to the reactor dome of the Angra 2 nuclear reactor near Rio de Janeiro, Brazil, at a position about 30 m from the core of the 3.95 GW thermal power reactor, where the estimated antineutrino flux is $7.8 \times 10^{12}\,\overline{\nu}/\mathrm{cm}^2/\mathrm{s}$ [44]. The experiment had an initial engineering run in 2014 for commissioning and background characterisation [45], before installing 14 scientific CCDs in 2016. The analysis of $2016-2018$ data resulted in an upper limit on the CEνNS rate of about 40 times the SM expectation for the lowest energy region starting from 75 eV [44], which led to competitive limits on simplified NSI models with light scalar and vector mediators [46]. A hardware binning was applied at the readout stage in 2019 data, which enabled us to lower the detection threshold to 50 eV and obtain new CEνNS limits [47].

In 2021, two Skipper-CCDs [48] were installed in the CONNIE detector with the aim of further decreasing the detection threshold to record low levels. These novel, ultra-low-noise sensors allow to measure for the first time the reactor energy spectrum down to a threshold of 15 eV. The resulting improvement in sensitivity at low energies is employed to search for CEνNS, as well as rare processes beyond the SM.

This work reports the first results from the CONNIE experiment with Skipper-CCDs, based on an analysis of the data set recorded in 2021 and 2022. This text is organised as follows. Section II describes the CONNIE experiment detector with Skipper-CCDs and the data set, Section III outlines the data processing and calibration procedures, and Section IV shows the detector performance, event selection and the resulting energy spectra with the reactor on and off. These are applied in three searches for rare processes in Section V: the Standard-Model coherent elastic neutrino-nucleus scattering, neutrino NSIs mediated by a light vector particle, and dark-matter diurnal modulations. The concluding remarks and prospects are given in Section VI.

II. THE CONNIE DETECTOR WITH SKIPPER-CCDS

In order to achieve the sensitivity to low energies required for detecting CEνNS, it is essential to minimize the readout noise and, consequently, reduce the detection energy threshold of the sensors as much as possible. The recently developed Skipper-CCDs [48] operate with a nondestructive output readout stage that can sample multiple times the charge in each pixel. In this way, the readout noise which is added by the output amplifier is reduced to sub-electron levels and sensitivity to individual electrons is achieved, allowing to count the exact number of electrons in each pixel. Skipper-CCD sensors are employed to search for dark matter by the SENSEI [49], DAMIC-M [50] and OSCURA [51] experiments, in the SOAR spectrograph instrument [52], at the Atucha reactor [43] and in precise studies of silicon properties [53, 54]. In July 2021 two Skipper-CCDs were

installed in the CONNIE detector, making it the first experiment to employ these novel sensors for reactor neutrino detection.

II.1. Experimental setup and commissioning

The CONNIE sensors are two identical fully-depleted silicon Skipper-CCDs of 675 μm thickness, designed at LBNL in collaboration with FNAL during the R&D phase of the SENSEI experiment [49] and fabricated at Teledyne DALSA Semiconductor. They are made from high-resistivity ($\sim$18 kΩ-cm) n-type silicon substrate, with a p-type buried channel implant and without backside processing. Each sensor is segmented into 1022×682 pixels of 15×15 μm^2 size, giving an area of 1.57 cm^2 and a mass of 0.247 g.

The sensor is connected to a dedicated Kapton flex-cable with micro-wire bonds, glued to a 7×7 cm^2 silicon substrate and packaged in a two-piece copper tray, identical to the ones used for the CONNIE standard CCDs, as shown in the left photo of Fig. 1. The two Skipper-CCD packages were installed in the lowest slots of the copper box that holds the sensors in the detector, while the 14 standard CCDs from the previous CONNIE setup remained in their original positions (Fig. 1 center). The Skipper-CCD flex cables connect through new dedicated second-stage flex circuits with signal preamplification to the vacuum side of a newly designed vacuum-interface board (Fig. 1 right), which transfers the signals from the two Skipper-CCDs and two standard CCDs. From the air-side of the interface, the signals are taken to four Low-Threshold-Acquisition (LTA) readout boards [55] using long flat cables.

The rest of the detector setup is unchanged with respect to the previous operations [44, 47]. The sensors operate in a vacuum of 10^{-7} torr and are cooled to below 100 K to minimise thermally-generated dark current. The detector is surrounded by passive shielding, including 15 cm of lead to absorb photons and two 30-cm layers of high-density polyethylene to shield against cosmogenic neutrons. After the installation, the experiment took data for commissioning from mid-July to early November 2021, when the full passive shielding was assembled. Since then, the data acquisition has been continuous until the end of 2023, with short interruptions due to technical issues, on-site interventions or power cuts.

II.2. Data acquisition

The best operational configuration of the 2 Skipper-CCDs in terms of the quality of the acquired images was achieved by measuring half of each sensor using one of the 4 output amplifiers located in its corners. The data acquisition cycle consists of two phases: cleaning and readout. During cleaning, a procedure to reduce surface dark current is performed, in which the sensor surface voltages are reversed [56]. Then, after setting the voltages to their usual operation values, the charge in the CCD active area is clocked and discarded during several minutes, so that the readout starts with a "clean" CCD. The readout is done sequentially by alternating the phasing of the vertical clocks, so that the charge in the row of pixels adjacent to the serial register is first moved into it. Subsequently, the entire row of pixels is retrieved as the charge is sequentially shifted through the amplifier in the serial register, guided by another set of three voltages known as the horizontal clocks.

Both sensors are read out simultaneously with $N_{skp} = 400$ samples per pixel, thus taking approximately 2 hours to acquire a raw image and resulting in a nonuniform exposure in different pixels. The data-taking periods are divided into runs, which are usually sets of $\sim$500 images that share a common detector configuration and operation conditions. The current data set contains 300 days of data, collected between November 2021 and December 2022, from which 243 days were taken with the reactor on. There were two periods when the reactor was off: from June 12 to July 25, 2022 and from November 10 to 29, 2022, during which a total of 57 days of reactor-off data were collected.

III. DATA PROCESSING

The raw images are two-dimensional FITS images [57] in which each N_{skp} consecutive pixels in the same row correspond to the N_{skp} performed measurements of the charge of the same pixel. The first process applied to the raw images in arbitrary digital units (ADU). The horizontal baseline is computed for each row of the processed image as the median of the pixels in the overscan (unexposed) region, while the vertical baseline is computed in each column as the median of the first 100 pixels in the column. The horizontal and vertical baselines are subtracted row by row and column by column, respectively.

Due to the Skipper-CCD readout noise achieved with $N_{skp} = 400$ samples/pix reaching a fraction of an electron (the measured value is $0.15\,\mathrm{e}^-$, as detailed in Section IV.1), the consequent charge distribution of the images is a sequence of Gaussian peaks with the means centered on multiples of the electron charge, as shown in Fig. 2. This indivitual electron resolution of the sensors [48] is used to calibrate the image from ADU to number of electrons.

III.1. Energy calibration

In order to establish a precise calibration for all the images in a run, a two-step procedure was implemented. Firstly, a rapid image-by-image calibration is conducted by fitting two Gaussian functions over the first two peaks, corresponding to 0 and 1 electrons. In this manner, a gain (in ADU/e$^-$) is determined from the difference be-

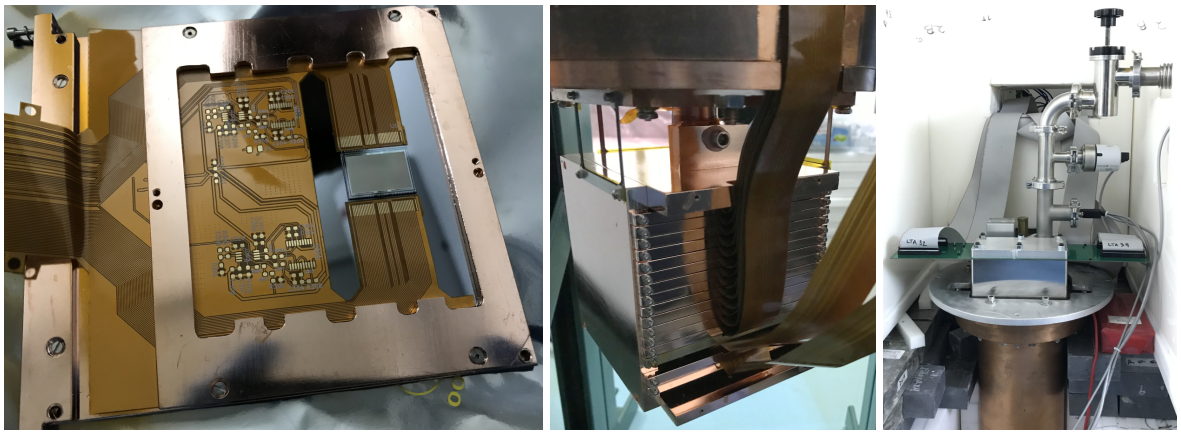

FIG. 1. CONNIE: Packaged Skipper-CCD (left), copper cold box with 14 standard CCDs and 2 Skipper-CCDs installed in the bottom positions (center), and vacuum interface board on top of the copper vacuum vessel (right).

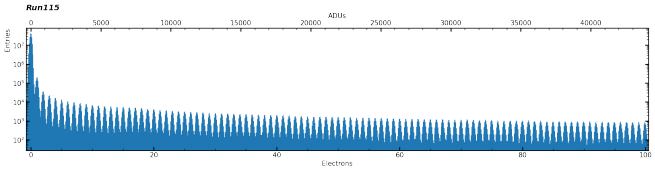

FIG. 2. Distribution of charge up to one hundred electron peaks in the data from one run.

tween the Gaussian means. Monitoring gain stability helps identify pathological images, which are excluded from the second part of the calibration, which involves determining a global constant for each run.

In the second step, the pixel charge distributions are summed to increase the data sample size in the electron peak distributions. By summing all the good images of a run, it becomes possible to observe more than 100 electron peaks with good resolution (see Fig. 2), and the information from all available peaks is taken into account by fitting them with independent Gaussian distributions. Finally, a linear fit is applied to the obtained Gaussian means to derive the global gain from the slope and the baseline residual correction from the intercept. The nonlinearity obtained with this method in the energy range of interest is less than 1%, in good agreement with previous works [53].

III.2. Size-to-depth calibration

When a pointlike energy deposition within the CCD volume produces a number of charge carriers (holes), the electric field present in the bulk causes them to drift towards the potential wells at the pixel top surface of the CCD where they are collected. As they drift, the holes diffuse laterally in the plane perpendicular to the drift direction (z). As shown in Ref. [58], the lateral spread is Gaussian with a variance that depends on the time the

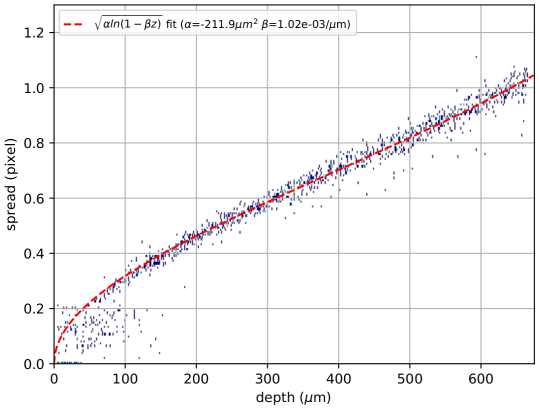

FIG. 3. Size-to-depth calibration curve from a sample of 45 muons in one Skipper-CCD.

holes are allowed to diffuse before being collected, which is proportional to the depth of the ionisation event. Holes produced close to the CCD back side have more time to diffuse before being collected and, therefore, they spread more than the holes produced close to the collection wells.

The size-to-depth calibration curve is determined from muon tracks using the same procedure as in standard CCDs [47]. Cosmogenic muons pass through the CCD leaving a straight track which is narrow at the entry point at the top of the CCD and widens as it progresses towards the back surface, where it exits. A sample of muon tracks perpendicular to the horizontal register is used to determine the lateral spread as a function of depth. Since the muon trajectory is a straight line, and the thickness of the CCD is known, a depth can be assigned to each muon slice and therefore to each value of the lateral spread, hence composing the calibration curve. The behavior of the size-to-depth relation from a sample of 45 muons in one sensor and one typical run is plotted in Fig. 3. Each point is a measurement of the size and depth of one slice of a muon track. The fitted curve $\sqrt{\alpha \ln(1-\beta z)}$ with pa-

rameters $\alpha = -212\ \mu\mathrm{m}^2$, $\beta = 1.02 \times 10^{-3}\mu\mathrm{m}^{-1}$, shown by the red dashed curve, gives the spread in μm, with variations of up to 4% between sensors and runs. It is known that the event size also depends on the energy deposit per pixel and that the muon curves slightly overestimate the event size at a given depth for low-energy deposits from neutrino interactions, as the muon energy deposits are more spread out due to the charge repulsion effect, compared with the small energy deposits by neutrinos that undergo diffusion only [58].

III.3. Masking

Due to the sub-electron noise, an order of magnitude lower than standard CCDs, the Skipper-CCD sensors have a high image resolution, making it possible to spot artifacts of charge smearing and defective pixels that can mimic low-energy events from diffusion-limited hits and become a background soure. To eliminate these features, a masking procedure to correctly flag these background events in the images was developed using reactor-off data and empty images formed by reading out serial registers without movement of pixel charges, and was applied prior to the event extraction.

The features, known as serial-register events (SRE), manifest in the images as charge deposits along a single row, originating from charge diffusion in the inactive silicon region that extends to the serial register. They frequently occur in clusters of adjacent pixels and occasionally in more dispersed arrangements along a single row. The latter may include isolated pixels reconstructed independently from the group of pixels associated with a single SRE, leading to potential misidentification as a diffusion-limited hit mimicking a neutrino event.

Consequently, for each image, an individual mask is generated in which entire rows with SRE candidates are marked for exclusion. The approach used to search for SRE candidates is based on the geometry of the charge distribution along a single row and requires the presence of at least two pixels in the same row, each with a minimum of $1.5\,\mathrm{e}^-$, not separated by more than two pixels, and with no adjacent pixels above and below with a charge greater than $1.5\,\mathrm{e}^-$. The threshold value of $1.5\,\mathrm{e}^-$ was chosen to exclude single-electron events, such as spurious charges or dark current [59]. The SRE identification algorithm was tested using images without events, by applying the event extraction (Section III.4) to these images with and without masks. The extraction efficiency was greater than 99%.

In addition to the SRE, another common background source in CCDs consists of hot pixels that produce bright columns and rows, or in some cases appear as individual hot pixels. These are identified by searching the image regions without particle tracks for rows or columns with more than 12 unmasked pixels with a charge greater than $0.6\,\mathrm{e}^-$. Also, to exclude hot features that appear frequently in a run, a single mask per run is built containing the flagged columns and rows that were found hot in more than 5% of the images. Furthermore, individual pixels that appear occupied with at least $2.56\,\mathrm{e}^-$, 16 times the readout noise, in more than 10% of the images in a run are also flagged as bad pixels. Merging the two hot pixel masks and the SRE individual masks results in an individual global mask for each image in a run.

The average fraction of pixels that were flagged in the global masks corresponds to 8% of the Skipper-CCDs (6% for one sensor and 10% for the other). The impact of the masking, concentrated on a few hot columns and rows, is a reduction by almost two orders of magnitude in the total charge.

III.4. Event extraction

Once the images are calibrated and masked, an event extraction procedure is applied to identify the pixel clusters associated to energy depositions and to create an event catalog for each image. The event extraction algorithm is the same as the one described in Ref. [44], but uses a charge threshold of 1.6 e^- (10σ above the noise level) for the seed pixel and of 0.64 e^- (4σ above the noise) for its adjacent pixels. These values were chosen in order to reconstruct the total event charge.

Additional event variables computed in the extraction algorithm are the widths σ_x and σ_y, obtained from a 2D Gaussian fit to the cluster charge distribution and giving information on the event shape and size. The coordinates of the barycenter position of the event in the image are also calculated as

$$x_{bary} = \frac{\sum_i x_i E_i}{\sum_i E_i} \qquad \text{and} \qquad y_{bary} = \frac{\sum_i y_i E_i}{\sum_i E_i}\,, \tag{1}$$

where (x_i, y_i) is the position of the $i-$th pixel in the event and E_i its energy. The subsequent data selection is performed on the image catalogs containing the event variables.

IV. SELECTION AND ENERGY SPECTRUM

IV.1. Data quality criteria

To establish a set of selection criteria for defining good-quality data, the performance of three parameters was analysed: the readout noise, the single-electron event rate and the number of flagged pixels in the global masks. The analysis was performed using only reactor-off data in order to establish a maximum limit for the parameters and exclude potentially compromised images.

The readout noise is the fluctuation added by the output amplifiers, while the single-electron events [59] are caused by spurious charge accumulated in the pixels due to spontaneous thermal emission or dark current, Cherenkov and recombination photons [60] or clock-

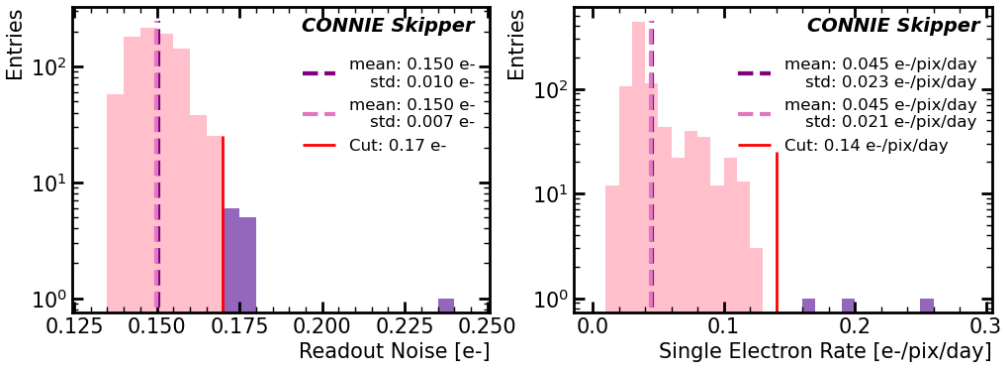

FIG. 4. (Left) Readout noise and (right) single-electron-rate distributions for reactor-off images. The purple histograms represent the whole sample, the purple dashed lines its mean, the red solid line the cut value and the pink histogram and dashed line the data kept after the cut.

induced charge [59]. Both the noise and the rate of single-electron events of each image are calculated during the data processing, and continuously monitored during data taking, together with the local gain. The procedure to compute the noise and single-electron rate is analogous to the one in the analysis of standard CCDs [47], by calculating the two parameters independently from the overscan and active regions, respectively. In order to exclude from the calculation pixels with large charges that do not represent sources of single-electron events, in addition to applying the SRE mask, all pixels with more than $5\,\mathrm{e}^-$ and a halo of 10 pixels around each are excluded from the active region in the calculation, leaving contributions from mostly pixels with 0 and 1 electrons.

Figure 4 shows the readout noise and single-electron-event rate distributions of one Skipper-CCD. The mean readout noise of the reactor-off data set is measured to be $(0.150 \pm 0.007)\,\mathrm{e}^-$. In order to exclude the outlier noisy images, only the ones with noise below $0.17\,\mathrm{e}^-$ are kept in the subsequent analysis. The single-electron rate is obtained as $(0.045 \pm 0.021)\,\mathrm{e}^-/\mathrm{pix/day}$. Since single-electron events can interfere significantly in the background rates, a cut is chosen to reduce these background sources, by keeping images with single-electron rate of less than $0.14\,\mathrm{e}^-/\mathrm{pix/day}$. Lastly, to ensure a good spatial coverage, images with more than 25% of masked pixels in the active region were excluded from the analysis. The effect of the data quality cuts is a reduction of 2.9% (5.6%) in the reactor-off (on) data sample.

IV.2. Event selection and exposure

After the data quality criteria, two event selection criteria are applied, based on the event positions within the active region and their shapes, in order to search for neutrino interactions in the sensor volume. The first is a geometrical cut, adopted from the previous analysis [47], that excludes the sensor borders of 10 pixels in the active region to avoid edge effects in the morphology of reconstructed events [61]. The result is a small reduction in the effective area of the sensor and is reflected in the total exposure.

The second is a selection cut based on the size of the events. Following the same approach as the analysis of standard CCDs [47], events are required to have widths σ_x and σ_y smaller than 0.95 pixels to exclude events that are large or come from the back CCD layer which has only partial charge collection and can produce fake low-energy events [62]. In addition, a lower limit of 0.2 pixels is set on the widths, considering the sensitivity of the reconstruction algorithm.

Since the Skipper-CCDs do not have an exposure time prior to the readout stage, a single pixel in the sensor is only exposed during the sequential readout of other pixels before it in the readout line. This is taken into account to calculate the effective exposure of each image. A time map is built assigning to the n-th pixel an exposure time $t_{exp} = t_{ro}(n-1)/(N_{pix}-1)$, where t_{ro} is the total image readout time and N_{pix} is the total number of pixels in the image. By removing all the regions excluded in the geometrical cut and the individual global mask, the image exposure time is designated as the average exposure time of the remaining pixels in the time map.

IV.3. Detection efficiency

The detection efficiency determination uses the same methodology as in previous analyses [44, 47] by simulating 40 neutrino-like events per image from the reactor-off period, with a uniform probability in the active volume and a uniform energy distribution between 5 and 2005 eV, using the depth-size calibration based on muon tracks. Comparing the energy and 3D position of the simulated events before and after the image processing and event extraction, it was found out that almost all events were extracted with ∼100% acceptance. A small fraction, less than 1.3%, of simulated events generated traces similar to serial-register events and were flagged

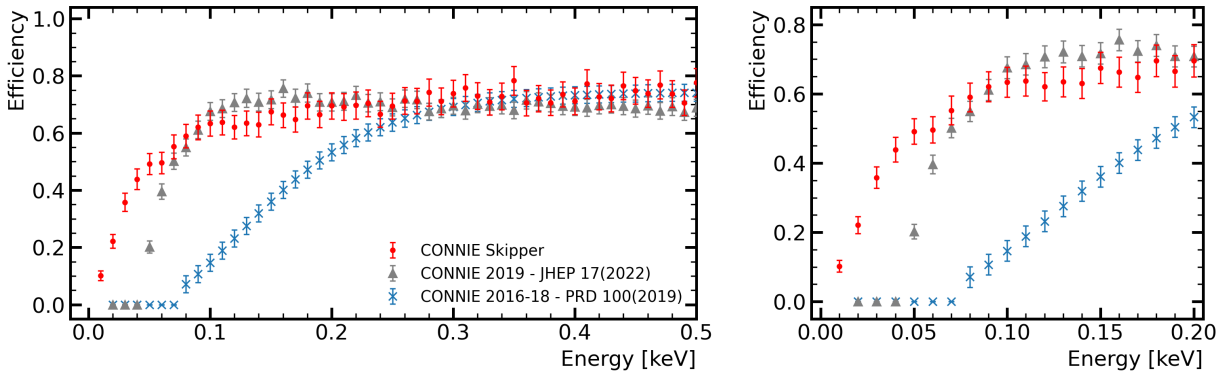

FIG. 5. CONNIE Skipper-CCDs detection efficiency (red), accounting for the event extraction acceptance and the selection cuts. The CONNIE standard CCD efficiencies from 2016-18 [44] (blue) and 2019 [47] (grey) are shown for reference. (Left) Efficiency up to energies of 0.5 keV and (right) a zoom into the low-energy region.

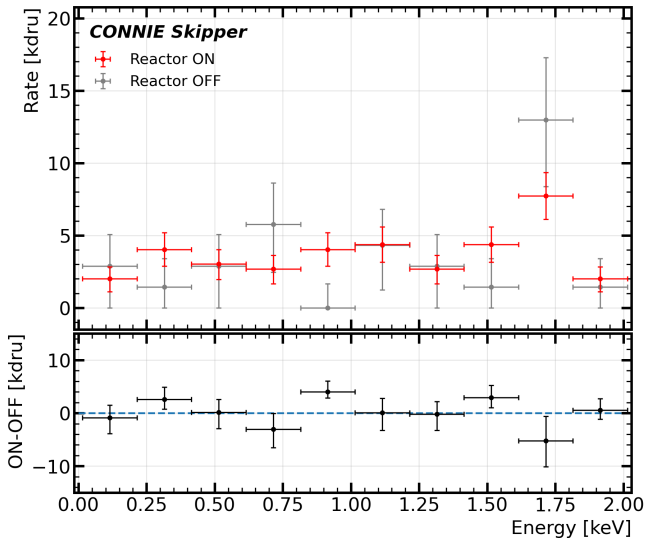

FIG. 6. (Top) CONNIE Skipper reactor-on and reactor-off spectra and (bottom) their difference.

by the masking routine, Section III.3.

The overall detection efficiency, shown in Fig. 5, accounts for the event extraction acceptance and the selection cuts. Compared to the previous runs with standard CCDs, the new sensors extend their efficient operation to lower energies and reach full efficiency around 100 eV, gaining a significant improvement. Based on this, the energy threshold for rare event searches was reduced to 15 eV, thus achieving the lowest energy threshold among all the current CEνNS experiments.

IV.4. Energy spectrum

All the processing, data quality and event selection criteria were fixed before unblinding the reactor-on data. The events that pass all selection cuts correspond to an effective exposure of 3.5 g-days with the reactor-off and 14.9 g-days with the reactor-on.

The resulting event rate distributions of the energy spectra for the selected events over the two periods, accounting for their effective exposure, are shown in Fig. 6 (details in Appendix A). The mean event rates are comparable at approximately 4 kdru, and are consistent with the previous analyses [44, 45, 47]. The difference between the reactor-on and off energy spectra is also shown, demonstrating no significant excess. Nevertheless, due to the record low energy threshold and the low single-electron-event rates, the current data set can be employed to search for rare processes in and beyond the SM.

V. SEARCHES FOR RARE PROCESSES

V.1. Search for coherent elastic neutrino-nucleus scattering

In order to obtain the expected neutrino rates at the detector, the SM neutrino coherent interaction rates are corrected for the effects of selection efficiency and resolution, obtained from simulation, as well as for the quenching factor that represents the fraction of nuclear recoil energy that creates ionisation. Here a similar procedure is used as the one in Ref. [63].

The predicted antineutrino flux at the detector is calculated following the summation method described in [64–67], updated with improved antineutrino spectra for the fissile isotopes ^{235}U, ^{238}U, ^{239}Pu and ^{241}Pu. The contribution from activation (neutron capture) of structural and fuel elements relevant for energies below 1.27 MeV

was also updated following [68]. The detection threshold of 15 eV_{ee} corresponds to a minimum observable neutrino energy of ∼0.44 MeV, according to the Sarkis quenching factor model [69]. Above this energy, the updated flux model and the one used previously [63] agree to within 3% and are thus considered equivalent in this analysis (details can be found in Appendix A).

The detection efficiency discussed in Section IV.3 is used as a multiplicative correction to the expected event rate as a function of the measured ionisation energy, E_M. For the quenching factor, $f_n(E_{\rm nr}) = E_I/E_{\rm nr}$, with E_I the ionisation energy, we use the updated model of Sarkis *et al.* [69], which allows to calculate the ionisation efficiency for nuclear recoil energies in silicon down to 0.05 keV_{nr}. This model, based on the original ideas by Lindhard [70], incorporates improved descriptions of the electronic stopping, interatomic potential and electronic binding at sub-keV energies, covering the Skipper-CCD low-energy range ($E_{\rm nr} > 0.240$ keV_{nr}) corresponding to events above the 0.015 keV_{ee} threshold. The energy resolution $R(E_I, E_M)$ is modeled as a Gaussian with variance $\sigma^2 = \sigma_0^2 + F_e E_{eh} E_I$, where $\sigma_0 = 3.04$ eV_{ee} is the readout noise, $F_e = 0.119$ is the electronic Fano factor, and $E_{eh} = 3.752$ eV_{ee} is he mean energy to create an electron-hole pair in silicon [71].

The resulting predicted rates for the CEνNs spectrum for Skipper-CCDs are shown in Table I, using the same binning as the data. A comparison with the Chavarria quenching factor [72], valid for $E_{\rm nr} > 0.30$ keV_{nr}, and out of range for Skipper-CCD data near the threshold, is also given for reference. The uncertainties in the expected rates take into account systematic variations due to the quenching factor [69, 72], efficiency (see Appendix B for details) and reactor budget [66, 73].

Based on the difference between the measured reactor-on and off event rates in Fig. 6, a 95% confidence-level (C.L.) upper limit on the observed event rate is established [74, 75], shown in the third column of Table I. The observed limit in the lowest-energy bin, where the expected rates are highest, lies at 76 times the SM prediction using the Sarkis quenching factor [69]. The expected limits are also calculated and shown in the last column of the table. Comparing the results for the observed limit obtained with Skipper-CCDs and the previous result using standard CCDs [47], they are of similar size. This can be explained by the fact that, on one hand, the sensitivity on the current limit is restricted by the large rate uncertainties due to the low exposures, while on the other hand it benefits from the significant improvement in detection efficiency at low energies. This enhanced sensitivity motivates the need to increase sensor mass in order to harness the full potential of Skippers-CCDs in the search for CEνNS with reactor neutrinos.

V.2. Search for new light vector mediator with CEνNS detection channel

Theories beyond the SM that include light mediators are highly motivated by the experimental results in various fields of particle physics [79–82], including dark matter and neutrino physics. New mediators can be probed under the framework of the so-called "simplified models" which, accounting only for representative new particles and interactions, allow to characterise new physics with a small number of parameters [83]. Reactor neutrino experiments, sensitive to low-energy interactions, have demonstrated their competitiveness in constraining new light mediators in the mass region below ∼10 MeV [46, 78].

Here, the CONNIE results from the Skipper-CCD run are employed to constrain the parameter space of a light vector mediator Z' in the framework of the simplified universal model [76], using the CEνNS detection channel. Considering the lowest energy bin, between 15 eV and 215 eV, the expected event rate in CONNIE, $R_{SM+Z'}$, is computed when accounting for the presence of the new mediator in addition to the SM interactions. The exclusion region in the phase space of the Z' mass ($M_{Z'}$) and coupling ($g_{Z'}$) is then calculated as the one in which this rate is greater than the observed upper limit on the event rate at the 95% C.L. for the same energy bin.

Figure 7 (left) shows the resulting CONNIE limits from the Skipper-CCD run with the updated Sarkis (2023) quenching factor [69]. For illustration purposes, the limit corresponding to the Chavarria quenching factor is also given [72], although recent measurements and calculations suggest it may be less valid at such low energies. The exclusion regions derived from the CONNIE Skipper-CCDs improve slightly the bounds imposed with the CONNIE standard-CCDs using the Chavarria quenching factor [46], mostly as an effect of the updated quenching factor at low energies, and to a lesser extent because the significantly higher Skipper-CCD rate uncertainty is compensated by the lower threshold, which enhances their sensitivity. A comparison with other experimental results in Fig. 7 (right) shows that the new CONNIE limit is less stringent but approaches that based on the COHERENT experiment CEνNS detection with CsI+Ar and its own quenching factor measurement [77]. The limit is more stringent at low mediator masses compared to the CONUS experiment, which uses germanium detectors and the Lindhard model with a quenching parameter of $k = 0.16$ [78], thanks to the Skipper-CCD reach to lower energies.

Figure 7 (left) also shows the 95% C.L. upper limit projections assuming a zero difference between the reactor-on and off rates and a statistical error five times smaller in the lowest-energy bin. These limits may be achieved if CONNIE can collect 25 times more data by, for example, increasing its mass.

Measured Energy [keV$_{ee}$]	Sarkis (2023) rate [kg^{-1}d^{-1}keV$_{ee}^{-1}$]	Chavarria rate [kg^{-1}d^{-1}keV$_{ee}^{-1}$]	Observed 95% C.L. [kg^{-1}d^{-1}keV$_{ee}^{-1}$]	Expected 95% C.L. [kg^{-1}d^{-1}keV$_{ee}^{-1}$]
$0.015 - 0.215$	$29.3\,^{+4.6}_{-4.7}$	17.7 ± 3.3	2.24×10^3	3.18×10^3
$0.215 - 0.415$	$2.7\,^{+1.3}_{-1.2}$	2.20 ± 0.21	7.36×10^3	4.77×10^3
$0.415 - 0.615$	$0.43\,^{+0.41}_{-0.39}$	0.36 ± 0.04	3.41×10^3	3.31×10^3

TABLE I. Expected CEνNS event rates for different ionisation efficiency models considering the efficiency and resolution for Skipper-CCDs. In the last column the observed and the expected limit at 95% C.L. are tabulated.

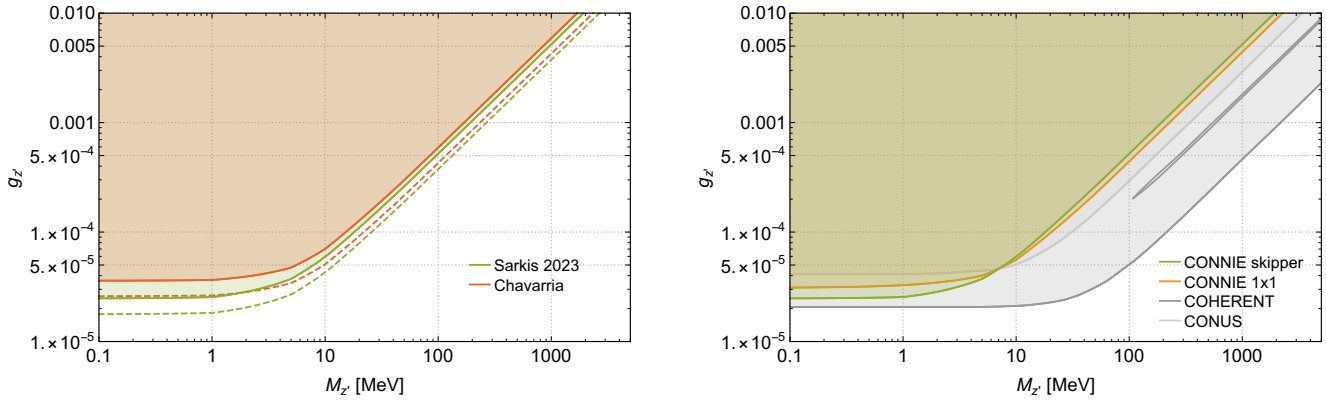

FIG. 7. (Left) CONNIE Skipper-CCD exclusion limits (solid lines) at the 95% C.L. from the CEνNS detection channel for a light vector mediator, assuming the simplified universal model [76], and considering quenching factors from Sarkis [69] (green) and Chavarria [72] (red); and projections of these limits (dashed) assuming a zero difference between the rates and a five times smaller statistical error. (Right) Comparison between CONNIE exclusion limits at the 95% C.L. from Skipper-CCDs (red) considering the quenching factor from Sarkis [69] (green) and the standard-CCD [46] (yellow). For comparison, limits at the 90% C.L. from COHERENT (CsI+Ar) [77] and CONUS ($k = 0.16$) data [78] are also shown.

V.3. Dark matter search by diurnal modulation

Dark matter (DM) direct detection experiments using Skipper-CCDs have the best current constraints for light dark matter candidates interacting with electrons in most of the energy range of interest ($0.5 - 1000$ MeV) [84, 86]. These constraints are limited in the lowest energy bin by the single-electron background rates. However, they can be improved by searching for a diurnal modulation, as explained in Ref. [87] and summarised below.

Due to the Solar System movement around the galaxy, there is a preferred direction of arrival of dark matter particles, which is known as the DM wind. This wind comes, on average, from the latitude 40° N. In the region of parameter space to which Skipper-CCDs are sensitive, DM particles interact with nuclei and electrons inside the Earth, and therefore can suffer elastic or inelastic collisions, producing a sidereal day modulation of their flux at the location of the detector. The "isodetection angle" is defined as the angle formed between the direction of the DM wind and the normal to the surface of the Earth at the detector location. Experiments located at the northern hemisphere scan low isodetection angles, meaning that the expected modulation is smaller (the DM particles only traverse the atmosphere and a small portion of the Earth crust in their trajectory). However, in the southern hemisphere, the isodetection angle spans over larger angles and the expected modulation becomes bigger. CONNIE is located at 23° S, allowing to scan a range of isodetection angles roughly between [65–161]°.

Stable single-electron-event rates are needed in order to look for the modulation. To that end, we limited this analysis to the most stable data taking run. Each image has an exposure of around one hour, and an average isodetection angle is assigned to it using the date and time information. The rates computed for each image are then binned in the isodetection angle. Simulations are carried out using DaMaSCUS [88, 89] to calculate the expected rate for each isodetection angle bin. The simulations are then compared to the measured rates and a 90% C.L. constraint for the DM parameters is calculated using a binned likelihood method.

The results are given in Fig. 8, considering models with MeV-scale DM, which couple to SM particles via a kinetically-mixed dark photon (A') [90, 91]. The plots show the DM phase space limits in terms of the DM particle mass (M_X) and its interaction cross-section with electrons (σ_e). The DM-electron scattering cross-section depends on the DM form-factor, $F_{\rm DM} = (\alpha m_e/q)^n$, with α the fine structure constant, m_e the electron mass and

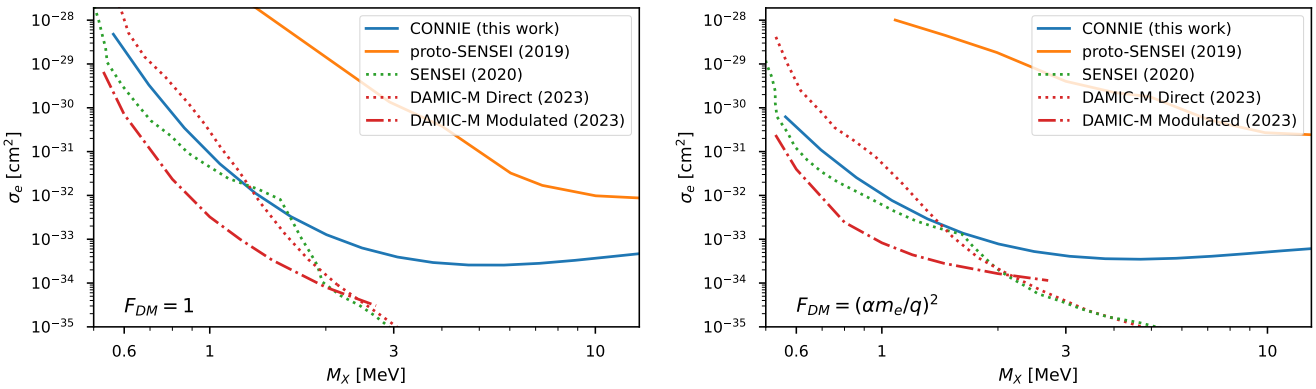

FIG. 8. 90% C.L. upper bounds on dark matter-electron interactions mediated by a heavy dark photon (left) and an ultralight dark photon (right) established by CONNIE (blue, solid), protoSENSEI [49] (orange, solid), SENSEI [84](green, dotted), and DAMIC-M (red, dashed for modulation searches [85] and red, dotted for direct searches[86]). Solid lines correspond to experiments running on the surface, dotted lines to direct limits obtained underground, and dashed to modulated limit obtained underground.

q the momentum transfer, which varies with the mediator mass, $M_{A'}$ [92]. For heavy dark photon mediators ($M_{A'} \gg \alpha m_e$) $n = 0$ and thus $F_{\rm DM} = 1$, while for ultralight mediators ($M_{A'} \ll \alpha m_e$), $n = 2$. The limits for the heavy and ultralight dark photon mediators are given in the left and right plots, respectively.

The figure also presents a comparison with other experiments. The plots in solid lines correspond to surface-level experiments, while dashed lines indicate underground experiments. In the $[0.6 - 10]$ MeV region, our analysis establishes the best limits for a surface-level experiment by 1–3 orders of magnitude in the DM-electron cross-section. Our limits are not competitive with underground experiments due to the cosmic background, which introduces extra single-electron events produced by effects such as Cherenkov radiation in silicon [60]. However, these are promising results for future searches in which a better stability of the detector is accomplished and the backgrounds are better understood.

VI. SUMMARY AND PROSPECTS

The CONNIE collaboration has successfully installed and commissioned two Skipper-CCDs in its detector, becoming the first experiment to employ these novel sensors with the aim to detect reactor neutrinos. The experiment took data between November 2021 and December 2022, demonstrating stable operation and low noise, and collecting a total data exposure of 18.4 g-days, after data quality selection. Despite the low exposure, resulting from the very low sensor total mass (0.25 g), the experiment achieved excellent sensor performance, with an ultra-low readout noise of $0.150\,e^-$, and a comparatively low single-electron rate, considering the surface location, of $0.045\,e^-$/pix/day. This allowed us to greatly improve the detection efficiency reach at low energies, achieving a record low threshold among all CEνNS experiments of 15 eV.

The current data set was investigated to look for rare processes, as a proof of principle for the possibilities of using Skipper-CCDs for searches within the SM and beyond. The sensitivity to CEνNS was extended to lower energies, where higher rates are expected, and the data analysis techniques improved in comparison to our previous results. Although the resulting CEνNS limit is not yet competitive, dominated by the statistical uncertainties of the small data set, it is comparable to our previous result, which was obtained using an exposure greater by two orders of magnitude. Thus, the results demonstrate an increased sensitivity to probing CEνNS and new neutrino interactions at very low energies, such as those predicted by some SM extensions with new light mediators. For simplified models with new light vector mediators, the limit in the phase space of the model represents an improvement to our previous result, which was obtained from a dataset with much larger exposure. In addition, a study of diurnal DM modulation was performed for the first time by CONNIE and the results denote the best limits on the DM-electron scattering cross-section, obtained by a surface-level experiment, representing an improvement by 1–3 orders of magnitude. These are the first results of analyses of Skipper-CCD data by CONNIE and demonstrate the robustness and versatility of the sensors, as well as their promising potential to detect CEνNS and probe new physics models with high sensitivity.

In order to succeed in measuring these rare processes, CONNIE must increase its active sensor mass, while maintaining the quality and stability of the performance. Considering as an example a 1-kg detector with the current noise, background rate and detection threshold, it would take only around a month to detect CEνNS at 90% C.L. The perspective for the immediate future

is to increase the mass by installing 16 new sensors, mounted in a compact arrangement on a Multi-Chip-Module (MCM), designed by Oscura [51]. The plan is to assemble the MCM inside the current CONNIE detector setup by mounting it in place of the copper box that now contains the standard and Skipper sensors. The rest of the detector design and shielding will be kept unchanged, to ensure minimal disruption to the overall setup and a speedy commissioning. This upgrade is planned for the first half of 2024 and will bring a 32-fold increase in sensor mass to a total of 8 g, thus greatly enhancing the physics potential of the CONNIE experiment.

ACKNOWLEDGEMENTS

We thank the Silicon Detector Facility staff at the Fermi National Accelerator Laboratory for hosting the assembly and test of the detector components used in the CONNIE experiment. The CCD development was partly supported by the Office of Science, of the U.S. Department of Energy under Contract No. DE-AC02-05CH11231. We are grateful to Eletrobras Eletronuclear, and especially to Ilson Soares, Israel Ottoni Simas and Livia Werneck Oliveira, for access to the Angra 2 reactor site, infrastructure and the support of their personnel to the CONNIE activities. We express our gratitude to Ronald Shellard (in memoriam) for supporting the experiment. We thank Marcelo Giovani for his IT support. We acknowledge the support from the Brazilian Ministry for Science, Technology, and Innovation and the Brazilian funding agencies FAPERJ (grants E-26/110.145/2013, E-26/210.151/2016, E-26/010.002216/2019, E-26/202.687/2019, E-26/210.079/2020), CNPq (grants 437353/2018-4, 407707/2021-2), and FINEP (RENAFAE grant 01.10.0462.00); Argentina's CONICET and AGENCIA I+D+i (grants PICT-2019-2019-04173; PICT-2021-GRF-TII-00458; PICT-2021-GRF-TI-00816) and Mexico's CONAHCYT (grant No. CF-2023-I-1169) and DGAPA-UNAM (PAPIIT grant IN104723). The UNAM group thanks Ing. Mauricio Martínez Montero for his technical assistance in skipper configuration studies. IN is also supported by a Latin American Association for High Energy, Cosmology and Astroparticle Physics Network (LAA-HECAP Network) grant through the ICTP Network Program. This work made use of the CHE cluster, managed and funded by COSMO/CBPF/MCTI, with financial support from FINEP and FAPERJ, and operating at the Javier Magnin Computing Center/CBPF.

Appendix A: Observed rates and expected neutrino flux

Table II shows the observed rates in bins of energy for data with the reactor on and off, and the difference between the two. The numbers correspond to the plot of Figure 6.

Energy range [keV]	Reactor-off rate [kdru]	Reactor-on rate [kdru]	Difference [kdru]
$0.015-0.215$	$2.9^{+2.2}_{-2.9}$	$2.0^{+0.8}_{-0.9}$	$-0.9^{+2.3}_{-3.0}$
$0.215-0.415$	$1.4^{+2.0}_{-1.4}$	$4.0^{+1.2}_{-1.2}$	$+2.6^{+2.3}_{-1.8}$
$0.415-0.615$	$2.9^{+2.2}_{-2.9}$	$3.0^{+1.0}_{-1.1}$	$+0.1^{+2.4}_{-3.1}$
$0.615-0.815$	$5.7^{+2.9}_{-3.3}$	$2.7^{+0.9}_{-1.0}$	$-3.0^{+3.0}_{-3.5}$
$0.815-1.015$	$0.0^{+1.7}_{-0.0}$	$4.0^{+1.2}_{-1.2}$	$+4.0^{+2.0}_{-1.2}$
$1.015-1.215$	$4.3^{+2.5}_{-3.1}$	$4.4^{+1.2}_{-1.2}$	$+0.1^{+2.8}_{-3.3}$
$1.215-1.415$	$2.9^{+2.2}_{-2.9}$	$2.7^{+0.9}_{-1.0}$	$-0.2^{+2.4}_{-3.1}$
$1.415-1.615$	$1.4^{+2.0}_{-1.4}$	$4.4^{+1.2}_{-1.2}$	$+3.0^{+2.3}_{-1.9}$
$1.615-1.815$	$13.0^{+4.3}_{-4.6}$	$7.7^{+1.6}_{-1.6}$	$-5.3^{+4.6}_{-4.9}$
$1.815-2.015$	$1.4^{+2.0}_{-1.4}$	$2.0^{+0.8}_{-0.9}$	$+0.6^{+2.1}_{-1.7}$

TABLE II. Observed rates with CONNIE Skipper-CCD reactor-on and reactor-off data, and the difference between the two.

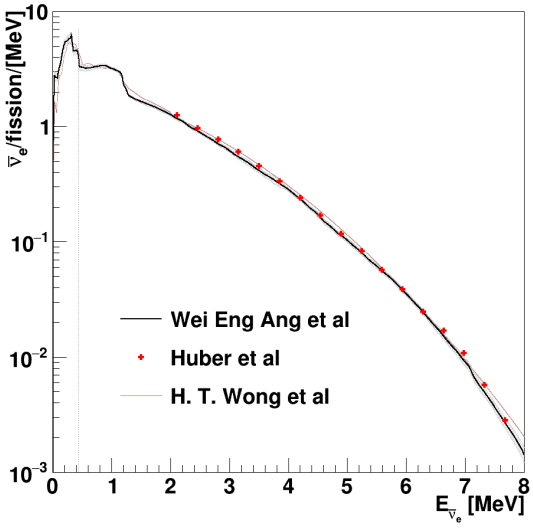

FIG. 9. Total reactor antineutrino spectrum per fission in the reactor per MeV for three models: (black) Wei Eng Ang *et al.* [64], (red) Huber *et al.* [93] and (brown) Wong [94]. The error band for Wei model is computed according to [66, 73]. The dotted vertical line denotes the neutrino energy threshold for Skipper-CCDs at CONNIE.

Figure 9 shows the updated antineutrino flux at the detector. It was calculated following the summation method described in [64–66], updated with improved antineutrino spectra for the fissile isotopes ^{235}U, ^{238}U, ^{239}Pu and ^{241}Pu, as well as with the contribution from activation (neutron capture) of structural and fuel elements relevant for energies below 1.27 MeV following [68]. The threshold of 15 eV_{ee} corresponds to a mini-

mum observable neutrino energy of ∼0.44 MeV, shown in the figure, according to the Sarkis quenching factor model [69]. Above this value, the updated flux model and the one used previously [63] agree to within 3% and are thus considered equivalent. The main difference between the new and old flux models appears for $E_\nu \lesssim 0.35$ MeV, which is below the minimum observable neutrino energy.

Appendix B: Fitting functions for detection and ionisation efficiency

To obtain and reconstruct the events registered during a Skipper-CCD exposure, a specific set of processing tools are used. The reconstruction efficiency for these tools has been evaluated using simulated events as it was discussed in section IV.3. This efficiency can be fitted by the continuous function,

$$\varepsilon(E_I) = b_0(1 - b_1 exp(-b_2(E_I)^4) - b_3 exp(-b_4 E_I)), \quad \text{(B1)}$$

where $b_0 = 0.763599$, $b_1 = 0.108047$, $b2 = 51.1075$, $b_3 = 0.984304$ and $b_4 = 26.0671$ for the central curve only, with a $\chi^2 = 20/95$, see fig. 10. For the upper efficiency curve the parameters are, $b_0 = 0.813653$, $b_1 = 0.115169$, $b_2 = 19.5823$, $b_3 = 0.955748$ and $b_4 = 26.5726$. And for the lower efficiency curve the parameters are, $b_0 = 0.717902$, $b_1 = 0.122821$, $b_2 = 19.9976$, $b_3 = 0.980065$ and $b_4 = 26.2413$.

For the ionisation efficiency we used the first principles model from [69], where we fit the continuous function,

$$f_n(E_R) = \frac{(a_1(E_R - E_0) + a_2(E_R - E_0)^{a_3} + a_4(E_R - E_0)^{a_5})}{(a_6(E_R - E_0) + a_7(E_R - E_0)^{a_8})}, \quad \text{(B2)}$$

from $E_R = 0.08$ keV to $E_R = 10.00$ keV such that the relative error from the exact numeric tabulated value is less than 1%, see Fig. 10. The fit parameters for the central curve are, $E_0 = -0.0386870$ (keV), $\mathrm{a}_1 = 1.35347$ (1/keV), $\mathrm{a}_2 = -0.794527$ $(1/\mathrm{keV}^{\mathrm{a}_3})$, $\mathrm{a}_3 = 0.982405$, $\mathrm{a}_4 = -0.461248$ $(1/\mathrm{keV}^{\mathrm{a}_5})$, $\mathrm{a}_5 = 0.987530$, $\mathrm{a}_6 = -0.911767$ (1/keV), $\mathrm{a}_7 = 1.64321$ $(1/\mathrm{keV}^{\mathrm{a}_8})$, and $a_8 = 0.946677$.

For the upper curve the fit parameters are, $E_0 = -0.0152147$ (keV), $a_1 = 0.205447$ (1/keV), $a_2 = -0.0122554$ $(1/\mathrm{keV}^{\mathrm{a}_3})$, $a_3 = 0.709046$, $a_4 = -0.0274662$ $(1/\mathrm{keV}^{\mathrm{a}_5})$, $a_5 = 0.649680$, $a_6 = -0.0331458$ (1/keV), $a_7 = 1.02803$ $(1/\mathrm{keV}^{\mathrm{a}_8})$, and $a_8 = 0.784991$. For the lower curve the fit parameters are, $E_0 = -0.0724154$ (keV), $a_1 = 0.526887$ (1/keV), $a_2 = 0.00140378$ $(1/\mathrm{keV}^{\mathrm{a}_3})$, $a_3 = 0.283309$, $a_4 = -0.241916$ $(1/\mathrm{keV}^{\mathrm{a}_5})$, $a_5 = 0.828205$, $a_6 = -0.289727$ (1/keV), $a_7 = 3.05516$ $(1/\mathrm{keV}^{\mathrm{a}_8})$, and $a_8 = 0.819846$.

[1] D. Z. Freedman, Coherent Neutrino Nucleus Scattering as a Probe of the Weak Neutral Current, Phys. Rev. D **9**, 1389 (1974).

[2] D. Akimov *et al.* (COHERENT), Observation of Coherent Elastic Neutrino-Nucleus Scattering, Science **357**, 1123 (2017), arXiv:1708.01294 [nucl-ex].

[3] D. Akimov *et al.* (COHERENT), First Measurement of Coherent Elastic Neutrino-Nucleus Scattering on Argon, Phys. Rev. Lett. **126**, 012002 (2021), arXiv:2003.10630 [nucl-ex].

[4] D. Akimov *et al.* (COHERENT), Measurement of the Coherent Elastic Neutrino-Nucleus Scattering Cross Section on CsI by COHERENT, Phys. Rev. Lett. **129**, 081801 (2022), arXiv:2110.07730 [hep-ex].

[5] *Neutrino Non-Standard Interactions: A Status Report*, Vol. 2 (2019) arXiv:1907.00991 [hep-ph].

[6] D. K. Papoulias *et al.*, Recent probes of standard and non-standard neutrino physics with nuclei, Front. in Phys. **7**, 191 (2019), arXiv:1911.00916 [hep-ph].

[7] M. Lindner, W. Rodejohann, and X.-J. Xu, Coherent Neutrino-Nucleus Scattering and new Neutrino Interactions, JHEP **03**, 097, arXiv:1612.04150 [hep-ph].

[8] J. B. Dent, B. Dutta, S. Liao, J. L. Newstead, L. E. Strigari, and J. W. Walker, Probing light mediators at ultralow threshold energies with coherent elastic neutrino-nucleus scattering, Phys. Rev. D **96**, 095007 (2017), arXiv:1612.06350 [hep-ph].

[9] Y. Farzan *et al.*, Probing neutrino coupling to a light scalar with coherent neutrino scattering, JHEP **05**, 066, arXiv:1802.05171 [hep-ph].

[10] O. G. Miranda, D. K. Papoulias, M. Tórtola, and J. W. F. Valle, Probing new neutral gauge bosons with $CE\nu NS$ and neutrino-electron scattering, Phys. Rev. D **101**, 073005 (2020), arXiv:2002.01482 [hep-ph].

[11] M. Cadeddu, N. Cargioli, F. Dordei, C. Giunti, Y. F. Li, E. Picciau, and Y. Y. Zhang, Constraints on light vector mediators through coherent elastic neutrino nucleus scattering data from COHERENT, JHEP **01**, 116, arXiv:2008.05022 [hep-ph].

[12] J. B. Dent, B. Dutta, D. Kim, S. Liao, R. Mahapatra, K. Sinha, and A. Thompson, New Directions for Axion Searches via Scattering at Reactor Neutrino Experiments, Phys. Rev. Lett. **124**, 211804 (2020), arXiv:1912.05733 [hep-ph].

[13] D. Aristizabal Sierra, V. De Romeri, L. J. Flores, and D. K. Papoulias, Axionlike particles searches in reactor experiments, JHEP **03**, 294, arXiv:2010.15712 [hep-ph].

[14] J. B. Dent, B. Dutta, S. Liao, J. L. Newstead, L. E. Strigari, and J. W. Walker, Accelerator and reactor complementarity in coherent neutrino-nucleus scattering, Phys. Rev. D **97**, 035009 (2018), arXiv:1711.03521 [hep-ph].

[15] T. S. Kosmas, D. K. Papoulias, M. Tortola, and J. W. F. Valle, Probing light sterile neutrino signatures at reactor and Spallation Neutron Source neutrino experiments, Phys. Rev. D **96**, 063013 (2017), arXiv:1703.00054 [hep-ph].

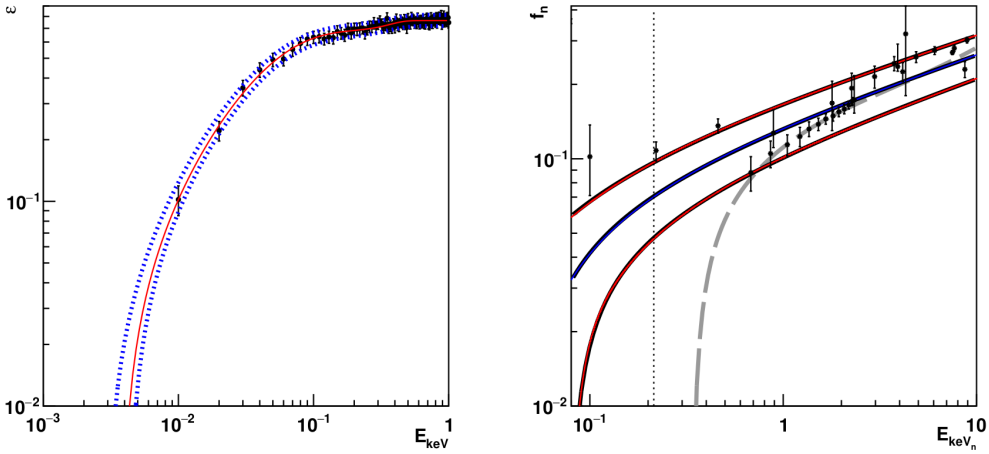

FIG. 10. (left) Efficiency points with error bars compared with the fit function from Eq. B1 (red). (right) Ionisation efficiency from [69] (blue), for the upper and lower curves (red) compared with the fit function from Eq. B2 (black) and from Chavarria [63] (long dash). The vertical dotted line shows the threshold recoil energy (0.24 $\mathrm{keV_n}$) for Skipper-CCDs using Eq. B2. Also shown are the measurements extracted from [69, 95].

[16] B. C. Cañas, E. A. Garcés, O. G. Miranda, and A. Parada, The reactor antineutrino anomaly and low energy threshold neutrino experiments, Phys. Lett. B **776**, 451 (2018), arXiv:1708.09518 [hep-ph].

[17] O. G. Miranda, D. K. Papoulias, O. Sanders, M. Tórtola, and J. W. F. Valle, Future CEvNS experiments as probes of lepton unitarity and light-sterile neutrinos, Phys. Rev. D **102**, 113014 (2020), arXiv:2008.02759 [hep-ph].

[18] A. Parada, Constraints on neutrino electric millicharge from experiments of elastic neutrino-electron interaction and future experimental proposals involving coherent elastic neutrino-nucleus scattering, Adv. High Energy Phys. **2020**, 5908904 (2020), arXiv:1907.04942 [hep-ph].

[19] M. Cadeddu, C. Giunti, K. A. Kouzakov, Y.-F. Li, Y.-Y. Zhang, and A. I. Studenikin, Neutrino Charge Radii From Coherent Elastic Neutrino-nucleus Scattering, Phys. Rev. D **98**, 113010 (2018), [Erratum: Phys.Rev.D 101, 059902 (2020)], arXiv:1810.05606 [hep-ph].

[20] O. G. Miranda *et al.*, Probing neutrino transition magnetic moments with coherent elastic neutrino-nucleus scattering, JHEP **07**, 103, arXiv:1905.03750 [hep-ph].

[21] R. Harnik, J. Kopp, and P. A. N. Machado, Exploring nu Signals in Dark Matter Detectors, JCAP **07**, 026, arXiv:1202.6073 [hep-ph].

[22] B. C. Cañas, E. A. Garcés, O. G. Miranda, and A. Parada, Future perspectives for a weak mixing angle measurement in coherent elastic neutrino nucleus scattering experiments, Phys. Lett. B **784**, 159 (2018), arXiv:1806.01310 [hep-ph].

[23] G. Fernandez-Moroni, P. A. N. Machado, I. Martinez-Soler, Y. F. Perez-Gonzalez, D. Rodrigues, and S. Rosauro-Alcaraz, The physics potential of a reactor neutrino experiment with Skipper CCDs: Measuring the weak mixing angle, JHEP **03**, 186, arXiv:2009.10741 [hep-ph].

[24] M. Cadeddu, N. Cargioli, F. Dordei, C. Giunti, Y. F. Li, E. Picciau, C. A. Ternes, and Y. Y. Zhang, New insights into nuclear physics and weak mixing angle using electroweak probes, Phys. Rev. C **104**, 065502 (2021), arXiv:2102.06153 [hep-ph].

[25] M. Hoferichter, J. Menéndez, and A. Schwenk, Coherent elastic neutrino-nucleus scattering: EFT analysis and nuclear responses, Phys. Rev. D **102**, 074018 (2020), arXiv:2007.08529 [hep-ph].

[26] D. Z. Freedman, D. N. Schramm, and D. L. Tubbs, The Weak Neutral Current and Its Effects in Stellar Collapse, Ann. Rev. Nucl. Part. Sci. **27**, 167 (1977).

[27] H.-T. Janka, Neutrino emission from supernovae, in *Handbook of Supernovae* (Springer International Publishing, 2017) pp. 1575–1604.

[28] J. Monroe and P. Fisher, Neutrino Backgrounds to Dark Matter Searches, Phys. Rev. D **76**, 033007 (2007), arXiv:0706.3019 [astro-ph].

[29] A. Gutlein *et al.*, Solar and atmospheric neutrinos: Background sources for the direct dark matter search, Astropart. Phys. **34**, 90 (2010), arXiv:1003.5530 [hep-ph].

[30] M. Bowen and P. Huber, Reactor neutrino applications and coherent elastic neutrino nucleus scattering, Phys. Rev. D **102**, 053008 (2020), arXiv:2005.10907 [physics.ins-det].

[31] B. K. Cogswell, A. Goel, and P. Huber, Passive Low-Energy Nuclear-Recoil Detection with Color Centers, Phys. Rev. Applied **16**, 064060 (2021), arXiv:2104.13926 [physics.ins-det].

[32] A. A. Aguilar-Arevalo *et al.* (CCM), First dark matter search results from Coherent CAPTAIN-Mills, Phys. Rev. D **106**, 012001 (2022), arXiv:2105.14020 [hep-ex].

[33] D. Baxter *et al.*, Coherent Elastic Neutrino-Nucleus Scattering at the European Spallation Source, JHEP **02**, 123, arXiv:1911.00762 [physics.ins-det].

[34] H. Bonet *et al.* (CONUS), Constraints on elastic neutrino nucleus scattering in the fully coherent regime from the CONUS experiment, Phys. Rev. Lett. **126**, 041804 (2021), arXiv:2011.00210 [hep-ex].

[35] I. Alekseev *et al.* (νGeN), First results of the νGeN experiment on coherent elastic neutrino-nucleus scattering, Phys. Rev. D **106**, L051101 (2022), arXiv:2205.04305 [nucl-ex].

[36] J. Colaresi, J. I. Collar, T. W. Hossbach, A. R. L. Kavner,

C. M. Lewis, A. E. Robinson, and K. M. Yocum, First results from a search for coherent elastic neutrino-nucleus scattering at a reactor site, Phys. Rev. D **104**, 072003 (2021), arXiv:2108.02880 [hep-ex].

[37] L. Singh *et al.* (TEXONO), Constraints on millicharged particles with low threshold germanium detectors at Kuo-Sheng Reactor Neutrino Laboratory, Phys. Rev. D **99**, 032009 (2019), arXiv:1808.02719 [hep-ph].

[38] D. Y. Akimov *et al.*, The RED-100 experiment, JINST **17** (11), T11011, arXiv:2209.15516 [physics.ins-det].

[39] J. J. Choi *et al.* (NEON), Exploring coherent elastic neutrino-nucleus scattering using reactor electron antineutrinos in the NEON experiment, Eur. Phys. J. C **83**, 226 (2023), arXiv:2204.06318 [hep-ex].

[40] G. Agnolet *et al.* (MINER), Background Studies for the MINER Coherent Neutrino Scattering Reactor Experiment, Nucl. Instrum. Meth. A **853**, 53 (2017), arXiv:1609.02066 [physics.ins-det].

[41] G. Angloher *et al.* (NUCLEUS), Exploring CEνNS with NUCLEUS at the Chooz nuclear power plant, Eur. Phys. J. C **79**, 1018 (2019), arXiv:1905.10258 [physics.ins-det].

[42] C. Augier *et al.* (Ricochet), Results from a prototype TES detector for the Ricochet experiment, Nucl. Instrum. Meth. A **1057**, 168765 (2023), arXiv:2304.14926 [physics.ins-det].

[43] E. Depaoli *et al.*, Deployment and performance of a Low-Energy-Threshold Skipper-CCD inside a nuclear reactor, (2024), arXiv:2401.07885 [hep-ex].

[44] A. Aguilar-Arevalo *et al.* (CONNIE), Exploring low-energy neutrino physics with the Coherent Neutrino Nucleus Interaction Experiment, Phys. Rev. D **100**, 092005 (2019), arXiv:1906.02200 [physics.ins-det].

[45] A. Aguilar-Arevalo *et al.* (CONNIE), Results of the Engineering Run of the Coherent Neutrino Nucleus Interaction Experiment (CONNIE), JINST **11** (07), P07024, arXiv:1604.01343 [physics.ins-det].

[46] A. Aguilar-Arevalo *et al.* (CONNIE), Search for light mediators in the low-energy data of the CONNIE reactor neutrino experiment, JHEP **04**, 054, arXiv:1910.04951 [hep-ex].

[47] A. Aguilar-Arevalo *et al.* (CONNIE), Search for coherent elastic neutrino-nucleus scattering at a nuclear reactor with CONNIE 2019 data, JHEP **05**, 017, arXiv:2110.13033 [hep-ex].

[48] J. Tiffenberg, M. Sofo-Haro, A. Drlica-Wagner, R. Essig, Y. Guardincerri, S. Holland, T. Volansky, and T.-T. Yu (SENSEI), Single-electron and single-photon sensitivity with a silicon Skipper CCD, Phys. Rev. Lett. **119**, 131802 (2017), arXiv:1706.00028 [physics.ins-det].

[49] M. Crisler, R. Essig, J. Estrada, G. Fernandez, J. Tiffenberg, M. Sofo haro, T. Volansky, and T.-T. Yu (SENSEI), SENSEI: First Direct-Detection Constraints on sub-GeV Dark Matter from a Surface Run, Phys. Rev. Lett. **121**, 061803 (2018), arXiv:1804.00088 [hep-ex].

[50] N. Castelló-Mor (DAMIC-M), DAMIC-M Experiment: Thick, Silicon CCDs to search for Light Dark Matter, Nucl. Instrum. Meth. A **958**, 162933 (2020), arXiv:2001.01476 [physics.ins-det].

[51] B. A. Cervantes-Vergara *et al.* (Oscura), Skipper-CCD sensors for the Oscura experiment: requirements and preliminary tests, JINST **18** (08), P08016, arXiv:2304.04401 [physics.ins-det].

[52] E. M. Villalpando *et al.*, Design of a Skipper CCD Focal Plane for the SOAR Integral Field Spectrograph (2022), arXiv:2210.03665 [astro-ph.IM].

[53] D. Rodrigues *et al.*, Absolute measurement of the Fano factor using a Skipper-CCD, Nucl. Instrum. Meth. A **1010**, 165511 (2021), arXiv:2004.11499 [physics.ins-det].

[54] A. M. Botti *et al.*, Constraints on the electron-hole pair creation energy and Fano factor below 150 eV from Compton scattering in a skipper CCD, Phys. Rev. D **106**, 072005 (2022), arXiv:2202.03924 [physics.ins-det].

[55] G. I. Cancelo *et al.*, Low Threshold Acquisition controller for Skipper CCDs, J. Astron. Telesc. Instrum. Syst. **7**, 015001 (2021), arXiv:2004.07599 [astro-ph.IM].

[56] S. E. Holland, D. E. Groom, N. P. Palaio, R. J. Stover, and M. Wei, Fully depleted, back-illuminated charge-coupled devices fabricated on high-resistivity silicon, IEEE Trans. Electron. Dev. **50**, 225 (2003).

[57] W. D. Pence, L. Chiappetti, C. G. Page, R. A. Shaw, and E. Stobie, Definition of the Flexible Image Transport System (FITS), version 3.0, A&A **524**, A42 (2010).

[58] M. Sofo Haro, G. Fernandez Moroni, and J. Tiffenberg, Studies on small charge packet transport in high-resistivity fully-depleted CCDs, IEEE Trans. Electron. Dev. **67**, 1993 (2020), arXiv:1906.11379 [physics.ins-det].

[59] L. Barak *et al.* (SENSEI), SENSEI: Characterization of Single-Electron Events Using a Skipper Charge-Coupled Device, Phys. Rev. Applied **17**, 014022 (2022), arXiv:2106.08347 [physics.ins-det].

[60] P. Du, D. Egana-Ugrinovic, R. Essig, and M. Sholapurkar, Sources of Low-Energy Events in Low-Threshold Dark-Matter and Neutrino Detectors, Phys. Rev. X **12**, 011009 (2022), arXiv:2011.13939 [hep-ph].

[61] J. Janesick, *Scientific Charge-coupled Devices*, Press Monograph Series (Society of Photo Optical, 2001).

[62] G. Fernandez-Moroni, K. Andersson, A. Botti, J. Estrada, D. Rodrigues, and J. Tiffenberg, Charge-Collection Efficiency in Back-Illuminated Charge-Coupled Devices, Phys. Rev. Applied **15**, 064026 (2021), arXiv:2007.04201 [physics.ins-det].

[63] G. Fernandez Moroni, J. Estrada, E. E. Paolini, G. Cancelo, J. Tiffenberg, and J. Molina, Charge coupled devices for detection of coherent neutrino-nucleus scattering, Phys. Rev. D **91**, 072001 (2015).

[64] W. E. Ang, S. Prasad, and R. Mahapatra, Coherent elastic neutrino nucleus scatter response of semiconductor detectors to nuclear reactor antineutrinos, Nucl. Instrum. Meth. A **1004**, 165342 (2021).

[65] L. Périssé, A. Onillon, X. Mougeot, M. Vivier, T. Lasserre, A. Letourneau, D. Lhuillier, and G. Mention, Comprehensive revision of the summation method for the prediction of reactor $\overline{\nu}_e$ fluxes and spectra, Phys. Rev. C **108**, 055501 (2023).

[66] A. Letourneau, V. Savu, D. Lhuillier, T. Lasserre, T. Materna, G. Mention, X. Mougeot, A. Onillon, L. Perisse, and M. Vivier, Origin of the reactor antineutrino anomalies in light of a new summation model with parametrized β^- transitions, Phys. Rev. Lett. **130**, 021801 (2023).

[67] R. Mills, B. Slingsby, J. Coleman, R. Collins, G. Holt, C. Metelko, and Y. Schnellbach, A simple method for estimating the major nuclide fractional fission rates within light water and advanced gas cooled reactors, Nuclear Engineering and Technology **52**, 2130 (2020).

[68] W. E. Ang, S. Prasad, and S. S. Chirayath, Antineutrino detection for temporal monitoring of fuel burnup in a large nuclear reactor, Nucl. Instrum. Meth. A **1028**, 166353 (2022).

[69] Y. Sarkis, A. Aguilar-Arevalo, and J. C. D'Olivo, Ionization efficiency for nuclear recoils in silicon from about 50 eV to 3 MeV, Phys. Rev. A **107**, 062811 (2023), arXiv:2209.04503 [physics.atom-ph].

[70] U. L. James F. Ziegler, J. P. Biersack, *The Stopping and Range of Ions in Solids*, ninth dover printing, tenth gpo printing ed. (Pergamon, 1985).

[71] D. Rodrigues, M. Cababie, I. G. Florenciano, A. Botti, J. Estrada, G. Fernandez-Moroni, A. M. Magnoni, M. Sofo Haro, J. Tiffenberg, and S. Uemura, Unraveling Fano noise and the partial-charge-collection effect in x-ray spectra below 1 keV, Phys. Rev. Applied **20**, 054014 (2023), arXiv:2305.09005 [physics.ins-det].

[72] A. E. Chavarria *et al.*, Measurement of the ionization produced by sub-keV silicon nuclear recoils in a CCD dark matter detector, Phys. Rev. D **94**, 082007 (2016), arXiv:1608.00957 [astro-ph.IM].

[73] L. Périssé, X. Mougeot, A. Onillon, and M. Vivier, Revised summation calculations of reactor antineutrino fluxes and spectra, in *International Conference on the Physics of the Two Infinities* (Kyoto, Japan, 2023).

[74] R. Barlow, Asymmetric errors, eConf **C030908**, WEMT002 (2003), arXiv:physics/0401042.

[75] R. Barlow, Asymmetric statistical errors, in *PHYSTAT (2005): Statistical Problems in Particle Physics, Astrophysics and Cosmology* (2004) pp. 56–59, arXiv:physics/0406120.

[76] D. G. Cerdeño, M. Fairbairn, T. Jubb, P. A. N. Machado, A. C. Vincent, and C. Bœhm, Physics from solar neutrinos in dark matter direct detection experiments, JHEP **05**, 118, [Erratum: JHEP 09, 048 (2016)], arXiv:1604.01025 [hep-ph].

[77] M. Atzori Corona, M. Cadeddu, N. Cargioli, F. Dordei, C. Giunti, Y. F. Li, E. Picciau, C. A. Ternes, and Y. Y. Zhang, Probing light mediators and $(g-2)_\mu$ through detection of coherent elastic neutrino nucleus scattering at COHERENT, JHEP **05**, 109, arXiv:2202.11002 [hep-ph].

[78] H. Bonet, A. Bonhomme, C. Buck, K. Fülber, J. Hakenmüller, G. Heusser, T. Hugle, M. Lindner, W. Maneschg, T. Rink, H. Strecker, and R. Wink, Novel constraints on neutrino physics beyond the standard model from the conus experiment, Journal of High Energy Physics **2022**, 10.1007/jhep05(2022)085 (2022).

[79] P. Fayet, U-boson production in e+ e- annihilations, psi and Upsilon decays, and Light Dark Matter, Phys. Rev. D **75**, 115017 (2007), arXiv:hep-ph/0702176.

[80] D. E. Kaplan, M. A. Luty, and K. M. Zurek, Asymmetric Dark Matter, Phys. Rev. D **79**, 115016 (2009), arXiv:0901.4117 [hep-ph].

[81] P. Langacker, The Physics of Heavy Z' Gauge Bosons, Rev. Mod. Phys. **81**, 1199 (2009), arXiv:0801.1345 [hep-ph].

[82] C. Giunti and A. Studenikin, Neutrino electromagnetic interactions: a window to new physics, Rev. Mod. Phys. **87**, 531 (2015), arXiv:1403.6344 [hep-ph].

[83] E. Morgante, Simplified Dark Matter Models, Adv. High Energy Phys. **2018**, 5012043 (2018), arXiv:1804.01245 [hep-ph].

[84] L. Barak *et al.* (SENSEI), SENSEI: Direct-Detection Results on sub-GeV Dark Matter from a New Skipper-CCD, Phys. Rev. Lett. **125**, 171802 (2020), arXiv:2004.11378 [astro-ph.CO].

[85] I. Arnquist *et al.* (DAMIC-M), Search for Daily Modulation of MeV Dark Matter Signals with DAMIC-M, Phys. Rev. Lett. **132**, 101006 (2024), arXiv:2307.07251 [hep-ex].

[86] I. Arnquist *et al.* (DAMIC-M), First Constraints from DAMIC-M on Sub-GeV Dark-Matter Particles Interacting with Electrons, Phys. Rev. Lett. **130**, 171003 (2023), arXiv:2302.02372 [hep-ex].

[87] X. Bertou *et al.*, Earth-Scattering Induced Modulation in Low-Threshold Dark Matter Experiments, in *XVIII International Conference on Topics in Astoparticle and Underground Physics (TAUP2023)* (Vienna, Austria, 2023).

[88] T. Emken and C. Kouvaris, DaMaSCUS: The Impact of Underground Scatterings on Direct Detection of Light Dark Matter, JCAP **10**, 031, arXiv:1706.02249 [hep-ph].

[89] T. Emken and C. Kouvaris, DaMaSCUS: Dark Matter Simulation Code for Underground Scatterings, Astrophysics Source Code Library, record ascl:1706.003 (2017).

[90] P. Galison and A. Manohar, TWO Z's OR NOT TWO Z's?, Phys. Lett. B **136**, 279 (1984).

[91] B. Holdom, Two U(1)'s and Epsilon Charge Shifts, Phys. Lett. B **166**, 196 (1986).

[92] T. Emken, R. Essig, C. Kouvaris, and M. Sholapurkar, Direct Detection of Strongly Interacting Sub-GeV Dark Matter via Electron Recoils, JCAP **09**, 070, arXiv:1905.06348 [hep-ph].

[93] P. Huber, Determination of antineutrino spectra from nuclear reactors, Phys. Rev. C **84**, 024617 (2011).

[94] H. T. Wong *et al.* (TEXONO), A Search of Neutrino Magnetic Moments with a High-Purity Germanium Detector at the Kuo-Sheng Nuclear Power Station, Phys. Rev. D **75**, 012001 (2007), arXiv:hep-ex/0605006.

[95] M. F. Albakry *et al.* (SuperCDMS), First Measurement of the Nuclear-Recoil Ionization Yield in Silicon at 100 eV, Phys. Rev. Lett. **131**, 091801 (2023), arXiv:2303.02196 [physics.ins-det].